A Parametric Blueprint for Optimum Cochlear Outer Hair Cell Design

Richard D. Rabbitt*[1,2,3] and Tamara C. Bidone[1,4,5,6]

[1]Biomedical Engineering, [2]Otolaryngology,[3]Neuroscience Program, [4]Molecular Pharmaceutics[5]Department of Biochemistry[6]Scientific Computing & Imaging Institute
University of Utah, 36 S Wasatch Drive, Salt Lake City, UT 84112.

*Corresponding author:
Richard D. Rabbitt
36 S. Wasatch Dr, SMBB 3100
Salt Lake City, UT. 84112
Ph: 801 581-6968
Email: r.rabbitt@utah.edu

Number of Pages: 18
Number of Figures: 4, tables 1, multimedia 0
Number of Citations: 59

Number of words: Abstract 248, Significance 117, Introduction 590, Results 2029, Discussion 1065, Methods 1451

Supplement: Mathematica Code including Derivations

Conflict of interest: The authors declare no competing financial interests.

Keywords: electromotility, prestin, cochlea, piezoelectricity, electro-mechanics, optimization, Hopf bifurcation, limit cycle oscillation, cell length, mechano-electrical transduction, control parameters, hearing frequency limit

Abstract. The present work examines the hypothesis that cochlear outer hair cell (OHC) length, membrane properties, and mechano-electrical transduction (MET) current vary in precise proportions along the cochlear tonotopic map to optimize electro-mechanical power conversion at each characteristic frequency (CF). We tested this hypothesis in a minimal model of OHC electro-mechanics that accounts for OHC biophysical properties as well as the cochlear mechanical load. Results identify three nondimensional ratios that maximize power conversion: the ratio of the resistive-capacitive (RC) corner frequency to CF, the ratio of nonlinear to linear capacitance, and the ratio of OHC stiffness to cochlear load stiffness. Optimum efficiency requires all three ratios to be universal constants quantitatively related to each other, independent of CF and species. From a dynamical systems perspective, the same three ratios are cardinal control parameters that combine to maximize power output by poising the OHC to operate on the edge of a dynamic instability, the critical point. Results support the hypothesis that OHC properties in extant species evolved to optimize electro-mechanical power conversion. Identification of the RC corner frequency as a dynamical control parameter that sets the critical point reveals a powerful mechanism used by medial olivocochlear efferent system to exert control over OHC stability and power output. Results further suggest the upper frequency limit of mammalian hearing is not constrained by the RC corner frequency or the speed of the motor, but instead is likely limited by the size of the nucleus and membrane surface area available for protein expression.

Significance Statement. Results provide strong evidence that evolutionary development of OHCs was driven by pressure to enhance electro-mechanical power conversion. Efficient power conversion requires specific OHCs properties that simultaneously match the cochlear load and poise the cell at the critical point. Results identify a parametric blueprint for optimum OHC design, which we posit applies across species and CFs. The blueprint reveals biophysical principles used by OHCs to amplify vibration across the entire bandwidth of mammalian hearing, including frequencies far exceeding what might be expected based on the low pass features of the membrane-motor complex measured in isolation. When applied to short OHCs of the odontocete cetaceans for example, the blueprint predicts peak power output at frequencies exceeding 100 kHz.

INTRODUCTION

The appearance of outer hair cells (OHCs) in the cochlea roughly 125 million years ago (Manley, 2012) endowed mammals with the ability to hear high frequency sounds, extending > 100kHz in whales and >70kHz in bats (Ketten, 1997; Davies et al., 2013). In contrast, hearing in reptiles, amphibians, lizards and fish is typically limited to < 2 kHz (Crawford and Fettiplace, 1980; Fay, 1995; Manley, 2017), and hearing in most birds is limited to < 8 kHz (Coles and Guppy, 1988; Duque et al., 2020). Across vertebrates there is an active process in inner ear sensory hair bundles that plays an important role in sensitivity {Martin, 2003 #158;Martin, 1999 #303;Martin, 2000 #124}, but the key difference in mammals is active electro-mechanical amplification by the cell body of cochlear OHCs (Brownell et al., 1985; Ashmore, 1987). Amplification is enabled by expression of the transmembrane protein prestin (Zheng et al., 2000), and manifested on the whole-cell level as a piezoelectric motor in the lateral wall membrane (Mountain and Hubbard, 1994; Zheng et al., 2002; He et al., 2014; Wang et al., 2016). The structure of prestin suggests motor function likely arises from voltage-driven conformational changes in the protein (Bavi et al., 2021; Ge et al., 2021; Butan et al., 2022), but the detailed molecular mechanism(s) underlying whole cell piezoelectricity remains a subject of research. Prestin is essential for sensitive hearing in mice over the 2-50 kHz range (Liberman et al., 2002; Cheatham et al., 2009), though prestin-independent electromotility has been implicated at frequencies >50kHz (Li et al., 2022). Direct electro-mechanical coupling in OHCs allows electrical power entering the cell primarily through the mechano-electrical transduction (MET) channels to be converted into mechanical power output, thereby drawing power from the electro-chemical endolymphatic potential to amplify vibrations in the cochlea. Although electrical charge displacement in prestin-expressing membrane patches (Gale and Ashmore, 1997; Santos-Sacchi and Tan, 2020) and voltage-driven whole-cell displacement (Frank et al., 1999; Santos-Sacchi and Tan, 2018) have low-pass characteristics, both electrical power consumption and mechanical power output are band-pass with best frequency exceeding 50kHz under some conditions (Rabbitt, 2022). It is currently not known if band-pass electro-mechanical power conversion in OHCs is tuned to the cochlear tonotopic map, or what role OHC biophysical properties play in setting the best power conversion frequency.

Monotonic variations in OHC biophysical properties along the tonotopic map provide a hint that each OHC might be tuned for best operation at a specific characteristic frequency (CF). Cells located at the 0.2 kHz CF place have a length of ~80 µm while cells located at the 10 kHz CF place have a length of ~40 µm (Dannhof et al., 1991; Pujol et al., 1992; Fettiplace, 2017). The correlation between OHC length and CF is universal across mammalian species, but precisely why the correlation exists is not known. Whole-cell OHC axial stiffness also varies with cell length (Iwasa and Adachi, 1997), and has an inverse log-linear scaling with CF similar to the stiffness of the in-tact cochlear partition (Naidu and Mountain, 1998). Passive capacitance and peak nonlinear capacitance both scale with cell length, roughly in proportion to the membrane surface area (Farrell et al., 2006; Corbitt et al., 2012), while basolateral ion channel expression and membrane conductance increases with CF (Housley and Ashmore, 1992; Johnson et al., 2011; Vavakou et al., 2019). Capacitance and conductance combine to cause the passive resistive-capacitive (RC) corner frequency of the cell membrane to increase with CF, which likely plays an important role in

amplification by shifting the timing of electro-mechanical force production (Nam and Fettiplace, 2012; Agarwal and Ramamoorthy, 2020). These correlations motivate the present hypothesis that specific properties are required for optimum OHC operation at CF. It has been suggested previously that OHC biophysical properties vary with CF to optimize impedance matching (Rabbitt et al., 2009; Rabbitt, 2020), or to set the OHC operating point near a dynamic instability (Camalet et al., 2000; Hudspeth et al., 2010; O Maoiléidigh and Hudspeth, 2013). Both hypotheses might be true, but the specific optimization problem that nature solved to specify OHC parameters remains unclear.

Here, we present theoretical evidence that OHC biophysical properties maximize electro-mechanical power conversion at CF, achieved by simultaneously matching the impedance of the OHC to the cochlear load *and* by poising the operating point of the cell on the stable edge of a dynamic instability. Results suggest OHCs evolved under rigid constraints relating OHC length and biophysical properties to each other and to the mechanics of the organ of Corti along the tonotopic map.

RESULTS

Concomitant OHC Properties Required to Optimize Power Conversion. We used the minimal model illustrated in Fig. 1 to examine electro-mechanical power conversion in OHCs. which includes biophysical properties of the OHC as well as the passive mechanical properties of the mechanical load in the cochlea. The active process includes only the prestin-dependent lateral wall motor and excludes contributions from hair bundle motility. The load consists of mass, stiffness and viscous drag acting on both ends of the cell. The system is driven by a force applied to the apical mass, representing sound-induced pressure in the cochlea. Amplification is powered by the mechano-electrical transduction (MET) current entering the cell, which is gated in proportion to cell displacement. The cochlear load is treated as linear, but the MET current and the piezoelectric coefficient both include saturating nonlinearities. A detailed mathematical description is provided in the Methods Section.

The model equations are nonlinear, self-excited, and unstable under certain conditions. Sensitivity of the MET current to cell displacement is a key parameter that determines the bifurcation point where the cell transitions from stable to unstable. In the present analysis we assume the OHC is poised at the edge of dynamic instability in order to maximize tuning and gain (Camalet et al., 2000; Hudspeth et al., 2010; O Maoiléidigh and Hudspeth, 2013). It is sufficient to use the linearized equations to find the MET current gains that place the OHC at the critical point where vibration is maximized (see Supplement for derivation). The optimum displacement gain σ at CF (ω_{cf}, rad-s^{-1}) is:

$$\sigma = -\omega_{cf}\frac{C}{\delta\ell}\left(\frac{\omega_{rc}}{\omega_{cf}}\frac{C_n}{C} + 2\zeta\left(\frac{r+1}{r}\right)\right), \tag{1}$$

the optimum velocity gain α is:

$$\alpha = \frac{G}{\delta\ell}\frac{2\zeta}{\omega_{cf}}\left(\frac{r+1}{r}\right), \tag{2}$$

giving the total mechanically-gated current as $i_M = \sigma x_1 + \alpha u_1$, where x_1 is the apical displacement and u_1 is the velocity. As detailed in the Methods and Table. 1, C is the linear capacitance, C_n is the nonlinear capacitance, δ is the piezoelectric strain coefficient, ℓ is the cell length, $\omega_{rc} = G/C$ is the passive RC corner frequency, G is the linearized membrane conductance, ζ is the nondimensional passive damping ratio and $r = \frac{k_c}{k_0}$ is the stiffness of the cochlear load k_c divided by the OHC axial stiffness k_0. In numerical simulations, we use the nonlinear gains σ_n and α_n at numerical time step "n" (see Methods), which reduce to Eq. 1-2 for small perturbations.

We call Eq. 1-2 the *critical point conditions* because they maximize tuning and gain by placing the system on edge of instability. This is equivalent to finding the gains that perfectly cancel the dissipative effects of viscosity and membrane conductance. It is significant to note appearance of three nondimensional ratios in these equations: the frequency ratio $\frac{\omega_{rc}}{\omega_{cf}}$, the stiffness ratio $r = \frac{k_c}{k_0}$, and the capacitance ratio $\frac{C_n}{C}$. All of three ratios can be controlled independently through gene expression, and all three are accessible for modification by natural selection. Since the ratios set the critical point, they are *control parameters* in the context of bifurcation theory (Ma and Wang, 2005).

When the system is at the critical point, membrane loss and damping are cancelled by the mechano-sensitive current, and the CF becomes equal to the undamped natural frequency. CF is found in the frequency domain from Eq. 6 for $\vec{f} = 0$. For the 1-DOF model we set $x_2 = 0$, $x_1 = x_0$, $k_1 \to k_0$, $m_1 \to m_0$, $b_1 \to b_0$, and solve for CF:

$$\omega_{cf} = \sqrt{\frac{k_c\left(1+\frac{C_n}{C}\right)+k_0}{m_0}}\,. \tag{3}$$

For the 2-DOF model we assume symmetric mass and viscous drag on the two ends of the cell ($m_1 = m_2, b_1 = b_2$), and write the mechanical stiffness at the basilar membrane in terms of the stiffness at the reticular lamina by $k_2 = \gamma k_1$. Solving for CF:

$$\omega_{cf} = \sqrt{\frac{1}{m_1}\left(\frac{1}{2}(\gamma k_1 + k_1 + 2k_c) + \frac{k_c C_n}{C} - k_c\sqrt{\left(\frac{C_n}{C}+1\right)^2 + \frac{k_1^2}{4k_c^2}(\gamma-1)^2}\right)}\,. \tag{4}$$

The optimum MET gains in Eqns. 1-2 are valid for both the 1-DOF and 2-DOF models providing the compliance of the total load is the same in both cases, which requires the stiffnesses to be related by: $k_0 = \left(\frac{1}{k_1} + \frac{1}{k_2}\right)^{-1} = \frac{k_1\gamma}{(\gamma+1)}$

The quality of the resonance is theoretically infinite in the linearized equations at CF if the mechano-sensitive gains are set according to Eqns. 1-2, but not all combinations of parameters result in the same power conversion efficiency. To find optimum parameters with highest efficiency, we minimized the total mechanically-gated current at CF with respect to cell length ℓ and membrane conductance G. In the optimization we approximated the linear

and nonlinear capacitance to be proportional to cell length (Corbitt et al., 2012), and stiffness to be inversely proportional to cell length (Iwasa and Adachi, 1997). Maximizing the efficiency requires the frequency ratio $\frac{\omega_{rc}}{\omega_{cf}}$ to be related to the stiffness ratio $r = \frac{k_c}{k_0}$ by:

$$\left(\frac{\omega_{rc}}{\omega_{cf}}\right)^2 = \frac{r-1}{r^2}, \tag{5}$$

and requires the capacitance ratio $\frac{C_n}{C}$ to be related to the damping ratio $\zeta = \frac{b_0}{b_{cr}} = \frac{b_0\omega_{cf}}{2(k_o+k_c)}$ and the stiffness ratio r by:

$$\left(\frac{C_n}{C}\right)^2 = 4\zeta^2\frac{(1+r)^2}{r^2(r-1)} \tag{6}$$

(see Supplement for derivation). We call Eqns. 5-6 the *impedance matched conditions*. The passive damping ratio $\zeta = \frac{b_0}{b_{cr}}$ can not be directly controlled by an individual OHC and therefore is termed extrinsic. The other three ratios $\left(\frac{\omega_{rc}}{\omega_{cf}}, \frac{k_c}{k_0}, \frac{C_n}{C}\right)$ can be controlled by OHC gene expression and therefore are termed intrinsic. Given the extrinsic damping ratio in the cochlea, Eqns. 5-6 place strong constraints on the OHC intrinsic ratios, because specifying any one of the three ratios determines the other two.

Mammals can manipulate the stiffness of the OHC through genes controlling the cytoarchitecture, and can independently manipulate the RC corner frequency though alternative genes controlling membrane conductance. Hence, by the mathematical principle of separation of variables, we conclude that both the right- and left-hand sides of Eq. 5 are constants, independent of CF and location in the cochlea. This means the ratios $\frac{\omega_{rc}}{\omega_{cf}}$ and $r = \frac{k_c}{k_0}$ are constants. The same reasoning applies to Eq. 6, and leads to the conclusion that that the left-and right-hand sides of Eq. 6 are constants. Since $r = \frac{k_c}{k_0}$ is a constant, we conclude that the ratios $\frac{C_n}{C}$ and $\zeta = \frac{b_0}{b_{cr}}$ are also constants independent of CF or species. It is also significant that the intrinsic ratios are the control parameters that set the critical point of maximum tuning and power output (Eqns. 1-2), and therefore are the key parameters that optimize OHCs for cochlear amplification.

To examine power amplification and the role of nonlinearity, we computed OHC electro-mechanical power conversion as a function of stimulus strength. Fig. 2A-F show results for the 1-DOF model for a 56μm long cell tuned to 3kHz CF, with properties set to the impedance matched values (Eqns. 1-6) listed in Table 1 (parameter set "C" unless otherwise noted). For nonlinear simulations (2A-D), equations were solved numerically and power was computed in the time domain (Eq. 12). Fig. 2A shows the time-average power delivered to the viscous load for sinusoidal forcing ranging from 1-1000 pN, normalized by force and frequency and plotted as power gain ($aW/nN^2/\sqrt{Hz}$). As the applied force becomes small (e.g.2A, 1pN, black curve, Eq. 17), the power gain delivered to viscosity in the nonlinear model becomes sharply tuned and equal to the power gain in the linear model (2A, gray

curve). The peak power output occurs for a stimulus frequency precisely at the 3kHz CF, and is attenuated ~4 orders of magnitude when the stimulus frequency is reduced to 2kHz. The best frequency decreases as the response transitions from active amplification (2A, black, 1pN) for low force levels to passive vibration for high force levels (2A, green, 1000pN). The mechanical power delivered to viscosity (2A) for low mechanical stimulus levels comes primarily from OHC electro-mechanical power conversion (2B, black curve, Eq. 16), and to a lesser extent from the applied mechanical force (2C, black curve, Eq. 15). As the magnitude of the sinusoidal force is increased the OHC begins to consume mechanical power rather than providing power (2B, dotted curves). At frequencies below CF, there is an interplay between OHC electro-mechanics and the applied force, resulting in highly inefficient delivery of power to overcome viscosity (2C, dotted curves). Fig. 2D shows the effect of the OHC nonlinearity on power output at 3kHz CF in the form of power gain vs. applied mechanical force magnitude, illustrating >3 orders of magnitude power amplification at low force levels relative to passive power delivery at high levels. For low force levels, numerical solutions of the full nonlinear system are identical to the linearized model.

We used the linearized model to examine parameter sensitivity, power distribution, and stability. Electro-mechanical power conversion (P_{em}, Eq. 16) is shown using the 1-DOF model for parameter set A (solid green, $\frac{\omega_{rc}}{\omega_{cf}} = 0.35$) and for parameter set B (solid blue, $\frac{\omega_{rc}}{\omega_{cf}} = 0.15$). Also shown for comparison is electro-mechanical conversion using the 2-DOF model for parameter set C (solid red, $\frac{\omega_{rc}}{\omega_{cf}} = 0.25$). OHC impedance matched ratios (Eqns. 5-6) and MET gains (Eqns. 1-2) were identical for 1-DOF and 2-DOF simulations. Similarity between the 3 curves in Fig. 2E is striking, and occurs because the OHC is impedance matched to the total load at 3kHz in all 3 simulations.

To illustrate how the power is distributed, Fig. 2F shows OHC electro-mechanical conversion (P_{em}, blue, Eq. 16), power delivered to viscosity (P_{out}, red, Eq. 17), power supplied by the applied force (P_m, green, Eq. 17), and power lost to the membrane conductance (P_{mem}, black dashed, Eq. 18). The dotted curve indicates the power is negative, but shown on the figure as the absolute value. As required from conservation of energy, the power delivered to viscosity is the addition of the electrical and mechanical terms: $P_{out} = P_{em} + P_m$. Fig. 2G shows electro-mechanical power conversion by OHCs ranging from 91 to 21 μm in length to illustrate the role of OHC length and CF.

Fig. 3 shows changes in stability and power output predicted by the linearized model when the control parameters deviate from their optimum values for a 56μm long OHC tuned to 3kHz CF. In all panels, the horizontal axis is the forcing frequency. Contour lines indicate positive OHC power output with contours equally spaced on a log scale. Regions lacking contour lines (Fig. 3, *) correspond to parameter space where the OHC consumes power rather than outputting power. Results are shown for the 1-DOF model (left) and the 2-DOF (right), with peak power output at the center of each panel (white horizontal line crossing 3kHz).

To poise the OHC at the critical point, the mechano-sensitive current must have a specific magnitude and phase (Eq. 1-2). Fig. 3A-B illustrates how power output and stability changes if the MET current gain (3A) or phase (3B) deviate from the critical point. If the MET gain (σ) is too small, the OHC consumes power instead of outputting power (3A,*). As the gain is increased the cell begins to output power (3A, white arrow), reaching a peak at the

critical point (3A, center). If the gain is above the critical point the system becomes unstable and enters a limit cycle oscillation (3A, red vertical bars). Stable power output is predicted only for a narrow range of gains, between the white arrows and white lines (4A). Results for the 1-DOF vs. 2-DOF linearized models are similar, with the 2-DOF model showing a modestly expanded region of stability. The optimum MET phase is shifted ~0.2 rad. relative to cell displacement (3B), and a change in phase reduces power output but does not lead to instability (3B).

The most efficient electro-mechanical power conversion requires the ratios $\frac{C_n}{C}$, $\frac{\omega_{rc}}{\omega_{cf}}$, and $\frac{k_c}{k_0}$ to be constants independent of CF (Eq. 5-6). Fig. 3. C-D illustrate how altering these ratios breaks the impedance match, changing power output and stability. Increasing prestin expression (C_n, Fig. 3C) reduces power output by pushing the best frequency above CF, and if significantly overexpressed can cause the cell to consume power rather than output power (3C, * regions without contour lines). Under-expression of prestin reduces power output primarily by pushing the best frequency below CF. Increasing the RC corner by increasing membrane conductance G is predicted to cause the cell to consume power rather than output power (3D, *), while decreasing the RC corner is predicted to induce instability (3D, red vertical bars) and lead to limit cycle oscillation. The present analysis predicts stable power output for a range of $\frac{\omega_{rc}}{\omega_{cf}}$, between the white arrow and white line (3D). Lowering the OHC axial stiffness below the stiffness of the cochlear partition (per OHC) is also predicted to lead to instability (3E, red vertical bars), while increasing stiffness reduces power output by pushing the best frequency above CF. Power output in the model is relatively insensitive to basilar membrane vs. reticular lamina stiffness, providing the combined stiffness is held at the impedance matched value (not shown).

DISCUSSION

Our results support the hypothesis that nature has optimized OHC electro-mechanical power conversion at CF by following a universal *parametric blueprint* of OHC design. The blueprint requires setting the MET gains at CF to satisfy the *critical point conditions* (Eqns. 1-4) and setting OHC biophysical parameters based on the nondimensional ratios $\frac{\omega_{rc}}{\omega_{cf}}$, $\frac{k_c}{k_0}$ *and* $\frac{C_n}{C}$ to satisfy the *impedance matching conditions* (Eq. 5-6). Importantly, the ratios are constants, independent of CF. The model is simplified and is not expected to capture fine details, but results clearly demonstrate that optimization of power conversion efficiency places stringent constraints on evolution of OHC properties.

Fig. 4 provides a summary of our main findings, and illustrates how OHC properties change with CF to optimize power conversion efficiency (Eqns 1-6). For the OHC lengths in Fig. 4A (Dannhof et al., 1991; Pujol et al., 1992; Fettiplace, 2017), optimum function as a motor requires linear capacitance C (4B, solid) and peak nonlinear capacitance C_n^{pk} (4B, dashed) to decrease linearly with log of CF, while maintaining the ratio $\frac{C_n^{pk}}{C}$ constant

(Eq. 5). The passive RC corner frequency (4C, dashed) is required to increase linearly with CF (4C, solid), while maintaining the ratio $\frac{\omega_{rc}}{\omega_{cf}}$ constant (Eq. 6). CF dependence of linear and nonlinear capacitance predicted here are consistent with data in guinea pig (Corbitt et al., 2012), and the requirement that the RC corner frequency falls well below CF is consistent with data from several species (Housley and Ashmore, 1992; Johnson et al., 2011; Vavakou et al., 2019). Optimization also requires the ratio $\frac{k_c}{k_0}$ to be a constant independent of CF (Eq. 5), which means the length of the OHC (4A) specifies both the OHC stiffness (4D, solid) (Iwasa and Adachi, 1997) and the stiffness of the cochlear load (per OHC) (4D, dashed). The stiffness increase is modest relative to CF, consistent with experimental measurements from the in-tact cochlear partition (Naidu and Mountain, 1998) and from isolated OHCs (Iwasa and Adachi, 1997). The analysis also predicts that the total mechanically-gated current increases with CF (Fig. 4E). The current gain in Fig. 4E is the sum of the MET current plus the mechanically-gated membrane current in the basolateral membrane, and is shown as pA per nm change in OHC length. There are no data currently available to directly test the prediction in Fig. 4E, but there is evidence that the single channel MET current increases substantially with CF (Fettiplace, 2009; Beurg et al., 2015), and that the expression of the ultrafast mechano-sensitive ion channel $K_v7.4$ also increases with CF (Perez-Flores et al., 2020), which we hypothesize combine to provide the net mechano-sensitive current predicted in Fig. 4E.

Present results further suggest the speed of OHC power output is not limited by the speed of the motor itself or the RC corner frequency, but instead is limited by the minimum possible cell length and maximum possible density of protein expression in the lateral wall. As CF increases, the OHC length must decrease (Fig. 4A), the basolateral membrane conductance must increase (Fig. 4B-C), and the mechanically gated current must increase (Fig. 4E). The minimum OHC length feasible to accommodate the nucleus and expression of required membrane proteins is about 8 µm, which places the upper limit of OHC peak power output near 115 kHz (Fig. 4A). Above this frequency, an 8µm long OHC can still output power but efficiency will be sharply attenuated (see Fig. 3G). Interestingly, a minimum OHC length near 8µm is consistent with short OHCs in toothed whales that hear above 100kHz (Ketten, 1997; Morell et al., 2015), and 115 kHz is close to the upper frequency estimated from behaviour for echolocating killer whales (Branstetter et al., 2017).

Physical parameters that set the mechano-sensitive current to its optimum value poise the OHC on the edge of a dynamic instability, a critical point responsible for the sharp tuning and high gain of OHCs under load (Camalet et al., 2000; Hudspeth et al., 2010; O Maoiléidigh and Hudspeth, 2013). Here, we used analytical methods to find closed form expressions locating the critical point in parameter space. There are three distinct *control parameters* that can push the system from optimum amplification into limit-cycle oscillation (Fig. 3, red vertical bars): increased sensitivity of mechano-sensitive current(s) (gain σ), decreased RC corner frequency (ratio $\frac{\omega_{rc}}{\omega_{cf}}$), and decreased OHC stiffness ratio ($\frac{k_c}{k_0}$). To illustrate the effect of changing a control parameter, Fig. 4F shows bifurcation from a stable linear system to nonlinear limit cycle oscillation caused by increasing the MET gain for a 56µm long OHC (3kHz CF). Above the bifurcation point (Fig. 3A), the OHC enters a self-sustaining stable limit-cycle oscillation (Fig. 4F) at a frequency ~5% below CF for the 56 µm long OHC. Changes in any of the three

control parameters can move the OHC away the critical point, resulting in decreased power output in one direction or limit cycle instability in the other direction.

Results demonstrating the RC corner frequency is a control parameter (through action on $\frac{\omega_{rc}}{\omega_{cf}}$) for dynamic stability has important implications regarding the function of the medial olivocochlear (MOC) efferent system. MOC synaptic contacts on OHCs modulate the conductance of the basolateral membrane (and ω_{rc}) through nicotinic acetylcholine receptors that trigger opening of Ca^{2+} activated K^{+} channels (Rohmann et al., 2015). Results in Fig. 3D show the OHC is unstable if ω_{rc} is too low, compelling the hypothesis that tonic firing of MOC efferent neurons sets the OHC at a stable operating point just above the bifurcation, which is the operating point of highest power output. Further increasing MOC efferent activity will push ω_{rc} above the optimum, eventually into a parameter space where the OHC consumes power rather than outputting power. Function as a control parameter for setting the operating point relative to the critical point gives the MOC system exquisite control over cochlear amplification, with the ability to influence power output well beyond what would be expected from a simple change in receptor potential modulation caused by an efferent mediated change in membrane conductance. This *control parameter* mechanism is likely responsible for the dramatic reduction of mechanical vibrations (Murugasu and Russell, 1996) and reduction in spiral ganglion neuron sensitivity (Wiederhold and Kiang, 1970; Guinan and Stankovic, 1996) caused by activation of the MOC system. MOC function as a control parameter is also consistent with the influence of contralateral acoustic stimulation on spontaneous otoacoustic emissions (SOAEs). Present results (Fig. 3D) predict a low OHC basolateral conductance can lead to instability and limit cycle oscillation (e.g. Fig. 4F), which would be manifested as a SOAE just below CF. Activation of the MOC by contralateral acoustic stimulation would increase the control parameter $\frac{\omega_{rc}}{\omega_{cf}}$ and move the operating point toward stability (Fig. 3D). Our numerical simulations predict MOC activation will reduce the SOAE amplitude and shift the frequency up, exactly as seen experimentally (Dewey et al., 2014).

MATERIALS AND METHODS

Time Domain Equations. The OHC is treated as a space clamped piezoelectric cell undergoing changes in length (Rabbitt, 2020). The membrane potential v_m is the addition of the resting voltage v_o plus a voltage perturbation v. For axisymmetric, isochoric deformations under turgor pressure, the piezoelectric shell equations (Yang and Batra, 1994) can be reduced to one dimension relating the OHC axial strain s to the axial force f_o and the transmembrane voltage perturbation v according to:

$$s = \kappa f_0 + \delta v, \tag{7}$$

where κ (N^{-1}) is the axial strain compliance and δ (V^{-1}) is the axial piezoelectric strain coefficient (δ is a nonlinear function of strain and voltage, see Appendix). The whole-cell axial displacement from the resting length ℓ (m) is the strain times the length $(x_1 - x_2) = s\ell$ (m). Solving for the force in the prestin-motor complex:

$$f_0 = k_c(x_1 - x_2) - \frac{\delta}{\kappa} v \tag{8}$$

where x_1 and x_2 are displacements of the apical and basal ends of the cell, $\frac{\delta}{\kappa}$ ($N\text{-}V^{-1}$) is the piezoelectric force coefficient, and k_c ($N\text{-}m^{-1}$) is the axial stiffness of the OHC which is related to the strain compliance κ (N^{-1}) and the length ℓ (m) by $k_c = 1/\kappa\ell$ (Iwasa and Adachi, 1997). The mechanical loads acting on the OHC at the apical and basal ends have effective stiffness k_n ($N\text{-}m^{-1}$), mass m_n (kg) and viscous drag b_n ($N\text{-}m^{-1}\text{-}s^{-1}$). Newton's second law for the apical load provides:

$$m_1 \frac{du_1}{dt} + b_1 u_1 + (k_1 + k_0)x_1 - k_o x_2 - \frac{\delta}{\kappa} v = f, \tag{9}$$

where f (N) is the force per OHC arising from the sound-induced dynamic pressure. The velocity at the apical end of the cell is $u_1 = \frac{dx_1}{dt}$ and the velocity at the basal end is $u_2 = \frac{dx_2}{dt}$. Newton's second law for the basal load provides:

$$m_2 \frac{du_2}{dt} + b_2 u_2 - k_o x_1 + (k_2 + k_0)x_2 + \frac{\delta}{\kappa} v = 0. \tag{10}$$

From Kirchhoff's current law for small deviations in voltage from the resting state (rest: v_o, i_o), the perturbation in voltage v is is related to the perturbation in current $i = i_M + i_e$ by

$$C \frac{dv}{dt} + Gv + \frac{\delta}{\kappa}(u_1 - u_2) - i_M = i_e \tag{11}$$

where C is the passive electrical membrane capacitance, G is the linearized membrane conductance from all ion channels, i_e is the electrode current (if any), and $i_M = i_{MET} + i_{MB}$ is the change in the total mechanically gated current including changes in the MET current from rest and mechano-sensitive basolateral ion channels. The total mechano-sensitive current is treated as a nonlinear function of apical displacement and velocity, and for simplicity we let the net mechanically gated current be $i_M = i_M(x_1, u_1)$ (see Appendix). In this model, the endolymphatic electro-chemical potential is the primary energy source, and cycle-by-cycle modulation of mechanically-gated current(s) provide all of the power for the motor.

The piezoelectric term $\frac{\delta}{\kappa}(u_1 - u_2)$ in Eq. 11 gives rise to nonlinear capacitance (NLC) (Rabbitt, 2020), which can be measured under voltage clamp conditions. The whole-cell NLC measured using *voltage clamp under zero load* is related to the piezoelectric strain coefficient δ, OHC length ℓ, and strain compliance by $= \ell^2/$ (see Appendix).

Matrix Equations. The piezoelectric stress coefficient $\eta_n = \frac{\delta}{\kappa}$ and the mechanically-gated current i_M are nonlinear saturating functions of OHC state and bundle deflection. The total current i_M includes the MET current plus current from strain-sensitive ion channels in the membrane (Perez-Flores et al., 2020). To facilitate stability analysis, we write the change in the mechanically-gated current in the form: $i_M = \sigma_n x_1 + \alpha_n v_1$. The gains σ_n and α_n are obtained from the nonlinear MET open probability, maximum conductance, electrochemical potential and membrane potential (Eqn. 23-25 below). With this, Eqns. 3-5 reduce to the matrix form

$$\frac{d\vec{w}}{dt} + \mathbf{M}\vec{w} = \vec{f} \tag{12}$$

where $\vec{w} = [x_1, x_2, u_1, u_2, v]^T$, the forcing vector $\vec{f} = [0,0, f/m_1, 0,0]^T$. The matrix **M** is

$$\boldsymbol{M} = \begin{bmatrix} 0 & 0 & -1 & 0 & 0 \\ 0 & 0 & 0 & -1 & 0 \\ (k_1 + k_c)/m_1 & -k_c/m_1 & b_1/m_1 & 0 & -\eta_n/m_1 \\ -k_c/m_2 & (k_2 + k_c)/m_2 & 0 & b_2/m_2 & \eta_n/m_2 \\ -\sigma_n/C & 0 & (\eta_n - \alpha_n)/C & -\eta_n/C & \omega_{rc} \end{bmatrix}. \tag{13}$$

The passive RC corner frequency in the absence of electromotility is defined as $\omega_{rc} = G/C$ (rad-s^{-1}). Eq. 6 is nonlinear due to dependence η_n, σ_n and α_n on membrane potential and cell displacement. The system is stable at the current state if the eigenvalues of **M** are positive.

The nonlinear equations were solved using the fifth-order Runge-Kutta-Fehlberg method implemented in Igor Pro (Wave Metrics, Lake Oswego, OR). The approach updated the piezoelectric stress coefficient η_n, and the displacement gain σ_n , and the velocity gain α_n at each numerical time step "n". In the linearized version of Eq. 6 the parameters η_n, σ_n and α_n are constants, and the solution is easily found in the frequency domain using:

$$\vec{W} = [j\,\omega\,\boldsymbol{I} + \boldsymbol{M}]^{-1}\,\vec{F}, \tag{14}$$

where upper case denotes the frequency domain. The linearized time and frequency domain variables are related by $f(t) = Fe^{j\omega t} + F^* e^{-j\omega t}$, $u_n(t) = U_n e^{j\omega t} + U_n^* e^{-j\omega t}$ and by $v(t) = Ve^{j\omega t} + V^* e^{-j\omega t}$, where the * indicates the complex conjugate

Electro-Mechanical Power Conversion. For the nonlinear model, the time-average mechanical power input by the applied force is computed in the time domain using:

$$p_m = \frac{1}{T}\int_0^T u_1 f dt, \tag{15}$$

which for small perturbations in the frequency domain becomes $P_m = \frac{1}{2}Re(U_1 F^*)$. From Eq. 5, the time-average electro-mechanical power conversion by the OHC is:

$$p_{em} = \frac{1}{T}\int_0^T \eta\ (u_1 - u_2)\ v\ \ dt \tag{16}$$

which for small perturbations in the frequency domain becomes $P_{em} = \frac{\eta}{2}Re((U_1 - U_2)\,V^*)$. From Eqns. 3-5, the time-average total power delivered by the applied force and the OHC to the viscous load is:

$$p_{out} = \frac{1}{T}\int_0^T (b_1 u_1^2 + b_2 u_2^2)\ \ dt = p_{em} + p_m \tag{17}$$

which for small perturbations in the frequency domain becomes $P_{out} = \frac{b_1}{2}U_1^2 + \frac{b_2}{2}U_2^2 = P_{em} + P_m$. The electrical power lost to OHC basolateral membrane conductance is:

$$p_{mem} = \frac{1}{T}\int_0^T G v^2 dt \tag{18}$$

which for small perturbations in the frequency domain becomes $P_{mem} = \frac{G}{2}V^2$.

From Eq. 11 it is clear that electromechanical power conversion is maximized when the phase of the shortening velocity is aligned with the phase of the voltage – which only occurs under specific "impedance-matched" conditions when the OHC biophysical parameters are optimized for power conversion efficiency.

Nonlinearities. The nonlinear capacitance C_n is related to the piezoelectric strain coefficient δ, the OHC length ℓ and the axial strain compliance κ according to

$$= \frac{e^2}{} = C_n^{pk}\varphi\ . \tag{19}$$

The saturating nonlinearity is defined here using a Langevin function

$$\varphi = 3\left(\frac{1}{\xi^2} - Csch(\xi)^2\right), \tag{20}$$

where

$$\xi = (v + v_o - v^{pk})/\lambda_v\ . \tag{21}$$

v_o is the resting potential and v^{pk} is the voltage of peak capacitance under resting stress. Present simulations use $\lambda_v = 0.032$ V (Santos-Sacchi et al., 1998).

Given the current state of the cell at time "n", the nonlinear piezoelectric stress coefficient η_n and piezoelectric strain coefficient δ_n are related to the peak nonlinear capacitance and voltage according to:

$$\eta_n = \frac{\delta_n}{\kappa} = \sqrt{\frac{C_n^{pk}\varphi}{\kappa\ell}}\ . \tag{22}$$

The nonlinear MET displacement gain σ_n given the current state of the cell at time "n" is

$$\sigma_n = \sigma g_n\left(v + v_o - v_{ep}\right)/\left(v_o - v_{ep}\right), \tag{23}$$

where v is the deviation in voltage away from the resting potential v_o ($v_m = v + v_o$ is the current membrane potential), v_{ep} is the endolymphatic potential, and σ is the optimum linear MET displacement gain from Eq. 1. The normalized displacement gain g_n at time "n" is found from the open probability (Howard and Hudspeth, 1988) to be

$$g_n = \frac{2\ e^{(x_o - x_1)/\lambda_x}}{1 + \left(e^{(x_o - x_1)/\lambda_x}\right)^2}, \tag{24}$$

where x_1 is the displacement of the apical end of the OHC and the saturation parameter is λ_x. Although λ_x varies with CF in the cochlea, the present simulations use λ_x =100 nm (Kennedy et al., 2005). The MET velocity gain given the current state of the cell at time "n" is written

$$\alpha_n = \alpha\frac{\sigma_n}{\sigma}, \tag{25}$$

where α is the optimum linear MET velocity gain from Eq. 2. The ratio $\frac{\sigma_n}{\sigma}$ causes the velocity gain to scale in proportion to the displacement gain, thereby maintaining the MET phase constant for sinusoidal stimuli irrespective of the magnitude of bundle displacement.

Parameters. Eqns. 1-6 place significant constraints on parameter selection. Voltage clamp data from guinea pig OHCs reported by Corbitt et al. (Corbitt et al., 2012) gives $\frac{C_n}{C}$ ≈0.89, which is nearly constant (s.d. 0.19; s.e.m. 0.03) for hair cells of various lengths across CF locations (~ 0.1- 40 kHz). The ratio of the passive RC corner frequency to CF also appears to be nearly constant, although specific values differ between reports. Data from gerbil and guinea pig OHCs place the ratio near $\frac{\omega_{rc}}{\omega_{cf}} \approx 0.15$ (Housley and Ashmore, 1992; Vavakou et al., 2019), while estimates from rat and gerbil OHCs place the ratio near $\frac{\omega_{rc}}{\omega_{cf}} \approx 0.36$ (Johnson et al., 2011). Present simulations therefore consider 3 parameter sets listed in Table 1, corresponding to $\frac{\omega_{rc}}{\omega_{cf}} \approx 0.15,\ 0.25$ and 0.36. Given the ratios $\frac{\omega_{rc}}{\omega_{cf}}$ and $\frac{C_n}{C}$, Eq. 5-6 are solved for the damping ratio $\zeta = \frac{b}{b_{cr}}$ and the stiffness ratio and $r = \frac{k_c}{k_0}$, which are also constants independent of CF For the 2-DOF model $r = \frac{k_c(\gamma+1)}{k_1\gamma}$. The mass m was found from ω_{cf}, using Eq. 3 for the 1-DOF model or Eq. 4 for the 2-DOF model. The OHC linear capacitance C was found from the cell membrane surface area using the linear equation in Table 1, which also specifies the peak nonlinear capacitance under zero load using the ratio $\frac{C_n}{C}$. Having the linear capacitance and the frequency ratio $\frac{\omega_{cf}}{\omega_{rc}}$ provides the membrane conductance G. The nonlinear capacitance and compliance provide the piezoelectric strain coefficient δ (Eq. 19). In the present simulations we set the mechano-sensitive current gains to 96% of the optimum values specified by Eqns. 1-2, to ensure the system was on the stable side of the critical point.

ACKNOWLEDGMENTS

The authors thank W. Brownell, K. Grosh, J.H. Nam and N. Soley for comments on portions of the manuscript. Funding was provided by the National Institutes on Deafness and other Communication Disorders grant R01 DC006685 (RDR) and the University of Utah (TCB).

TABLE 1. Optimum OHC Parameters

Paramater	Symbol	Value	Units	Based on
Parameter Set A				
Stiffness Ratio A	r	1.17	-	Eqns. 5-6
Frequency Ratio A	ω_{rc}/ω_{cf}	0.35	-	(Johnson et al., 2011)
Damping Ratio A	ζ	0.098	-	Eqns. 5-6
Parameter Set B				
Stiffness Ratio B	r	1.02	-	Eqns. 5-6
Frequency Ratio B	ω_{rc}/ω_{cf}	0.15	-	(Housley and Ashmore, 1992; Vavakou et al., 2019)
Damping Ratio B	ζ	0.035	-	Eqns. 5-6
Parameter Set C				
Stiffness Ratio C	r	1.07	-	Eqns. 5-6
Frequency Ratio C	ω_{rc}/ω_{cf}	0.25	-	Average A-B
Damping Ratio C	ζ	0.061	-	Eqns. 5-6
All Simulations				
Viscous Damping	b	$2\zeta(k_o + k_c)/\omega_{cf}$	N-s-m^{-1}	Definition
Linear Capacitance	C	$(10^{-12} + \ell \cdot 10^{-7}) \cdot 2.6$	F	(Corbitt et al., 2012)
Capacitance Ratio	C_n^{pk}/C	0.89	-	(Corbitt et al., 2012)
Conductance	G	$C\ \omega_{rc}$	S	$\omega_{rc} = G/C$
OHC Axial Stiffness	k_c	$1/\kappa\ell$	N-m^{-1}	(Iwasa and Adachi, 1997)
Total Load Stiffness	k_0	k_c/r	N-m^{-1}	$r = k_c/k_0$
Apical Stiffness	k_1	$k_0(\gamma + 1)/\ \gamma$	N-m^{-1}	Definition
Basal Stiffness	k_2	γk_1	N-m^{-1}	Definition
Length	ℓ	(7-3 Log(kHz)) $\cdot\ 10^{-5}$	m	(Dannhof et al., 1991; Pujol et al., 1992; Fettiplace, 2017)
Load Mass	m	from ω_{cf}	kg	Eqns. 3-4
NLC Peak V	v^{pk}	-0.045	V	(Santos-Sacchi et al., 1998)
Current vel. gain	α	calculated	A-s-m^{-1}	Eq. 2
Piezo Strain Coef.	δ	$\pm\sqrt{\kappa C_n/\ell}$	V^{-1}	Eq. 19
Apical/Basal Ratio	γ	10	-	(Dewey et al., 2019)
Strain Compliance	κ	$1.96 \cdot 10^6$	N^{-1}	(Iwasa and Adachi, 1997)
NLC Saturation	λ_v	0.032	V	(Santos-Sacchi et al., 1998).
Current Saturation	λ_x	100	nm	(Kennedy et al., 2005)
Current disp. gain	σ	calculated	A-m^{-1}	Eq. 1

Agarwal N, Ramamoorthy S (2020) Balance in the feedback loop component of the mammalian cochlear amplifier. J Applied Physics 128:034701.
Ashmore JF (1987) A fast motile response in guinea-pig outer hair cells: the cellular basis of the cochlear amplifier. J Physiol 388:323-347.
Bavi N, Clark MD, Contreras GF, Shen R, Reddy BG, Milewski W, Perozo E (2021) Prestin's conformational cycle underlies outer hair cell electromotility. Nature.
Beurg M, Xiong W, Zhao B, Muller U, Fettiplace R (2015) Subunit determination of the conductance of hair-cell mechanotransducer channels. Proc Natl Acad Sci U S A 112:1589-1594.
Branstetter BK, St Leger J, Acton D, Stewart J, Houser D, Finneran JJ, Jenkins K (2017) Killer whale (Orcinus orca) behavioral audiograms. J Acoust Soc Am 141:2387.
Brownell WE, Bader CR, Bertrand D, de Ribaupierre Y (1985) Evoked mechanical responses of isolated cochlear outer hair cells. Science 227:194-196.
Butan C, Song Q, Bai JP, Tan WJT, Navaratnam D, Santos-Sacchi J (2022) Single particle cryo-EM structure of the outer hair cell motor protein prestin. Nat Commun 13:290.
Camalet S, Duke T, Julicher F, Prost J (2000) Auditory sensitivity provided by self-tuned critical oscillations of hair cells. Proc Natl Acad Sci U S A 97:3183-3188.
Cheatham MA, Low-Zeddies S, Naik K, Edge R, Zheng J, Anderson CT, Dallos P (2009) A chimera analysis of prestin knock-out mice. J Neurosci 29:12000-12008.
Coles RB, Guppy A (1988) Directional hearing in the barn owl (Tyto alba). J Comp Physiol A 163:117-133.
Corbitt C, Farinelli F, Brownell WE, Farrell B (2012) Tonotopic relationships reveal the charge density varies along the lateral wall of outer hair cells. Biophys J 102:2715-2724.
Crawford AC, Fettiplace R (1980) The frequency selectivity of auditory nerve fibres and hair cells in the cochlea of the turtle. J Physiol 306:79-125.
Dannhof BJ, Roth B, Bruns V (1991) Length of hair cells as a measure of frequency representation in the mammalian inner ear? Naturwissenschaften 78:570-573.
Davies KT, Maryanto I, Rossiter SJ (2013) Evolutionary origins of ultrasonic hearing and laryngeal echolocation in bats inferred from morphological analyses of the inner ear. Front Zool 10:2.
Dewey JB, Lee J, Dhar S (2014) Effects of contralateral acoustic stimulation on spontaneous otoacoustic emissions and hearing threshold fine structure. J Assoc Res Otolaryngol 15:897-914.
Dewey JB, Applegate BE, Oghalai JS (2019) Amplification and Suppression of Traveling Waves along the Mouse Organ of Corti: Evidence for Spatial Variation in the Longitudinal Coupling of Outer Hair Cell-Generated Forces. J Neurosci 39:1805-1816.
Duque FG, Rodriguez-Saltos CA, Uma S, Nasir I, Monteros MF, Wilczynski W, Carruth LL (2020) High-frequency hearing in a hummingbird. Sci Adv 6:eabb9393.
Farrell B, Ugrinov R, Brownell W (2006) Frequency dependence of admittance and conductance of the outer hair cell. In: Auditory Mechanisms, Processes and Models (Nuttall A, Ren T, Gillespie K, Grosh K, de Boer E, eds), pp 231-232. New Jersey: World Scientific.
Fay RR (1995) Physiology of primary saccular afferents of goldfish: implications for Mauthner cell response. Brain Behav Evol 46:141-150.
Fettiplace R (2009) Defining features of the hair cell mechanoelectrical transducer channel. Pflugers Arch 458:1115-1123.
Fettiplace R (2017) Hair Cell Transduction, Tuning, and Synaptic Transmission in the Mammalian Cochlea. Compr Physiol 7:1197-1227.
Frank G, Hemmert W, Gummer AW (1999) Limiting dynamics of high-frequency electromechanical transduction of outer hair cells. Proc Natl Acad Sci U S A 96:4420-4425.
Gale JE, Ashmore JF (1997) The outer hair cell motor in membrane patches. Pflugers Arch 434:267-271.
Ge J, Elferich J, Dehghani-Ghahnaviyeh S, Zhao Z, Meadows M, von Gersdorff H, Tajkhorshid E, Gouaux E (2021) Molecular mechanism of prestin electromotive signal amplification. Cell 184:4669-4679 e4613.
Guinan JJ, Jr., Stankovic KM (1996) Medial efferent inhibition produces the largest equivalent attenuations at moderate to high sound levels in cat auditory-nerve fibers. J Acoust Soc Am 100:1680-1690.
He DZ, Lovas S, Ai Y, Li Y, Beisel KW (2014) Prestin at year 14: progress and prospect. Hear Res 311:25-35.

Housley GD, Ashmore JF (1992) Ionic currents of outer hair cells isolated from the guinea-pig cochlea. J Physiol 448:73-98.
Howard J, Hudspeth AJ (1988) Compliance of the hair bundle associated with gating of mechanoelectrical transduction channels in the bullfrog's saccular hair cell. Neuron 1:189-199.
Hudspeth AJ, Julicher F, Martin P (2010) A critique of the critical cochlea: Hopf--a bifurcation--is better than none. J Neurophysiol 104:1219-1229.
Iwasa KH, Adachi M (1997) Force generation in the outer hair cell of the cochlea. Biophys J 73:546-555.
Johnson SL, Beurg M, Marcotti W, Fettiplace R (2011) Prestin-driven cochlear amplification is not limited by the outer hair cell membrane time constant. Neuron 70:1143-1154.
Kennedy HJ, Crawford AC, Fettiplace R (2005) Force generation by mammalian hair bundles supports a role in cochlear amplification. Nature 433:880-883.
Ketten D (1997) Structure and Function in Whale Ears. Bioacoustics The International J of Animal Sound and its Recording 8:103-135.
Li J, Liu S, Song C, Zhu T, Zhao Z, Sun W, Wang Y, Song L, Xiong W (2022) Prestin-Mediated Frequency Selectivity Does not Cover Ultrahigh Frequencies in Mice. Neurosci Bull.
Liberman MC, Gao J, He DZ, Wu X, Jia S, Zuo J (2002) Prestin is required for electromotility of the outer hair cell and for the cochlear amplifier. Nature 419:300-304.
Ma T, Wang S (2005) Bifurcation theory and applications. Singapore ; Hackensack, N.J.: World Scientific.
Manley GA (2012) Evolutionary paths to mammalian cochleae. J Assoc Res Otolaryngol 13:733-743.
Manley GA (2017) Comparative Auditory Neuroscience: Understanding the Evolution and Function of Ears. J Assoc Res Otolaryngol 18:1-24.
Morell M, Lenoir M, Shadwick RE, Jauniaux T, Dabin W, Begeman L, Ferreira M, Maestre I, Degollada E, Hernandez-Milian G, Cazevieille C, Fortuno JM, Vogl W, Puel JL, Andre M (2015) Ultrastructure of the Odontocete organ of Corti: scanning and transmission electron microscopy. J Comp Neurol 523:431-448.
Mountain DC, Hubbard AE (1994) A piezoelectric model of outer hair cell function. J Acoust Soc Am 95:350-354.
Murugasu E, Russell IJ (1996) The effect of efferent stimulation on basilar membrane displacement in the basal turn of the guinea pig cochlea. J Neurosci 16:325-332.
Naidu RC, Mountain DC (1998) Measurements of the stiffness map challenge a basic tenet of cochlear theories. Hear Res 124:124-131.
Nam JH, Fettiplace R (2012) Optimal electrical properties of outer hair cells ensure cochlear amplification. PLoS One 7:e50572.
O Maoiléidigh D, Hudspeth AJ (2013) Effects of cochlear loading on the motility of active outer hair cells. Proc Natl Acad Sci U S A 110:5474-5479.
Perez-Flores MC, Lee JH, Park S, Zhang XD, Sihn CR, Ledford HA, Wang W, Kim HJ, Timofeyev V, Yarov-Yarovoy V, Chiamvimonvat N, Rabbitt RD, Yamoah EN (2020) Cooperativity of Kv7.4 channels confers ultrafast electromechanical sensitivity and emergent properties in cochlear outer hair cells. Sci Adv 6:eaba1104.
Pujol R, Lenoir M, Ladrech S, Tribillac F, Rebillard G (1992) Correlation Between the Length of Outer Hair Cells and the Frequency Coding of the Cochlea. In: Auditory Physiology and Perception (Cazals Y, Horner K, Demany L, eds), pp 45-52: Pergamon.
Rabbitt RD (2020) The cochlear outer hair cell speed paradox. Proc Natl Acad Sci U S A 117:21880-21888.
Rabbitt RD (2022) Analysis of outer hair cell electromechanics reveals power delivery at the upper-frequency limits of hearing. J R Soc Interface 19:20220139.
Rabbitt RD, Clifford S, Breneman KD, Farrell B, Brownell WE (2009) Power efficiency of outer hair cell somatic electromotility. PLoS Comput Biol 5:e1000444.
Rohmann KN, Wersinger E, Braude JP, Pyott SJ, Fuchs PA (2015) Activation of BK and SK channels by efferent synapses on outer hair cells in high-frequency regions of the rodent cochlea. J Neurosci 35:1821-1830.
Santos-Sacchi J, Tan W (2018) The Frequency Response of Outer Hair Cell Voltage-Dependent Motility Is Limited by Kinetics of Prestin. J Neurosci 38:5495-5506.
Santos-Sacchi J, Tan W (2020) Complex nonlinear capacitance in outer hair cell macro-patches: effects of membrane tension. Sci Rep 10:6222.
Santos-Sacchi J, Kakehata S, Takahashi S (1998) Effects of membrane potential on the voltage dependence of motility-related charge in outer hair cells of the guinea-pig. J Physiol 510 (Pt 1):225-235.
Vavakou A, Cooper NP, van der Heijden M (2019) The frequency limit of outer hair cell motility measured in vivo. Elife 8.

Wang Y, Steele CR, Puria S (2016) Cochlear Outer-Hair-Cell Power Generation and Viscous Fluid Loss. Sci Rep 6:19475.
Wiederhold ML, Kiang NY (1970) Effects of electric stimulation of the crossed olivocochlear bundle on single auditory-nerve fibers in the cat. J Acoust Soc Am 48:950-965.
Yang JS, Batra RC (1994) A Theory of Electroded Thin Thermopiezoelectric Plates Subject to Large Driving Voltages. J Appl Phys 76:5411-5417.
Zheng J, Madison LD, Oliver D, Fakler B, Dallos P (2002) Prestin, the motor protein of outer hair cells. Audiol Neurootol 7:9-12.
Zheng J, Shen W, He DZ, Long KB, Madison LD, Dallos P (2000) Prestin is the motor protein of cochlear outer hair cells. Nature 405:149-155.

FIGURE CAPTIONS

Fig. 1. Schematic of the model with a single-compartment piezoelectric OHC loaded by two spring-mass-damper systems.

Fig. 2. Electro-mechanical power conversion. All curves are normalized by sinusoidal applied force and shown as power gain in units of $aW/nN^2/\sqrt{Hz}$. With the exception of panel G, all all results are for a 56 µm long OHC (CF=3kHz). A-C). Predicted power gain for the non-linear model with the magnitude of the force ranging from 1-1000pN. A) Power delivered to viscosity (P_{out}, Eq. 12), B) OHC electro-mechanical power conversion (P_{em}, Eq. 11), and C) mechanical power associated with the sinusoidal force (P_m, Eq. 10). Dotted curves indicate negative power. D) Power gain at CF of 3kHz as a function of sinusoidal stimulus level showing compressive nonlinearity. E-G) Predicted power gain for the linear model. E) Electro-mechanical power conversion (p_{em}, Eq. 11) predicted by the 1-DOF linear model using parameter set "A" with ω_{rc}/ω_{cf}=0.35 (green, solid) and parameter set "B" with ω_{rc}/ω_{cf}=0.15 (blue, solid). Power conversion predicted by the 2-DOF linear model using parameter set "C" with ω_{rc}/ω_{cf}=0.25 (red, solid). The 2-DOF model shows a second resonance (*), but with a peak ~5 orders of magnitude less than the peak at CF. F) Components of power predicted by the 1-DOF linear model: electro-mechanical power conversion (blue, P_{em}), power delivered to viscosity (red, P_{out}, Eq. 12), power input by the applied force (green, P_m, Eq. 10), electrical power lost to membrane conductance (dashed, P_{mem}). Dotted curves indicate negative average power. G) Predicted electro-mechanical power conversion under impedance matched conditions for OHCs of various lengths for the 1-DOF model.

Fig. 3. Stability and power output. A-B) Changes in power output and stability with MET parameters for the 1-DOF (left) and 2-DOF (right) models for a 56 µm long cell located at 3 kHz CF (see Fig. 2). The 1-DOF and 2-DOF simulations use identical optimized parameters (Eqns, 14-18). A). Sensitivity of power output to MET magnitude with the optimum shown as the horizontal white line. Power output is shown on a log scale, with contour lines spaced equally on a log scale showing the region of positive power output to the viscous load. The critical point is located just above the white line in the center of the panels. The region above the white line leads to to stable limit cycle oscillations (vertical red bar), while the region between the white arrow and the white line leads to stable amplification. B) Sensitivity of power output to MET phase re: velocity. C-D) Changes in power output and stability with changes in OHC parameters. C) Sensitivity of power output to capacitance ratio, $\frac{C_n}{C}$. High levels of prestin expression and high C_n stiffen the system and ultimately cause the OHC to consume power (* regions) rather than output power. D) Sensitivity of power output to the ratio of the RC corner to CF, $\frac{\omega_{rc}}{\omega_{cf}}$. Power output is highly sensitive to ω_{rc} and stable power output occurs only over a limited range indicated between the white arrow and the horizontal white line. Since ω_{rc} is a control parameter for dynamic stability, changing its value has a large impact on power output. D). Sensitivity of power output to the stiffness of the OHC vs the load, $\frac{k_c}{k_0}$. Instability is predicted to occur if the OHC stiffness is too low.

Fig. 4. Summary of OHC parameters that poise the cell at the critical point and optimize electro-mechanical power conversion. A). OHC length vs. CF. B) Optimized linear and nonlinear capacitance. C) Optimized RC corner frequency. D) Optimized OHC stiffness. E) Optimized mechano-sensitive current (MET + K_v7.4). F) Transition from a stable linear response to limit cycle oscillation as a control parameter (MET gain in this example) pushes the system past the critical bifurcation point.

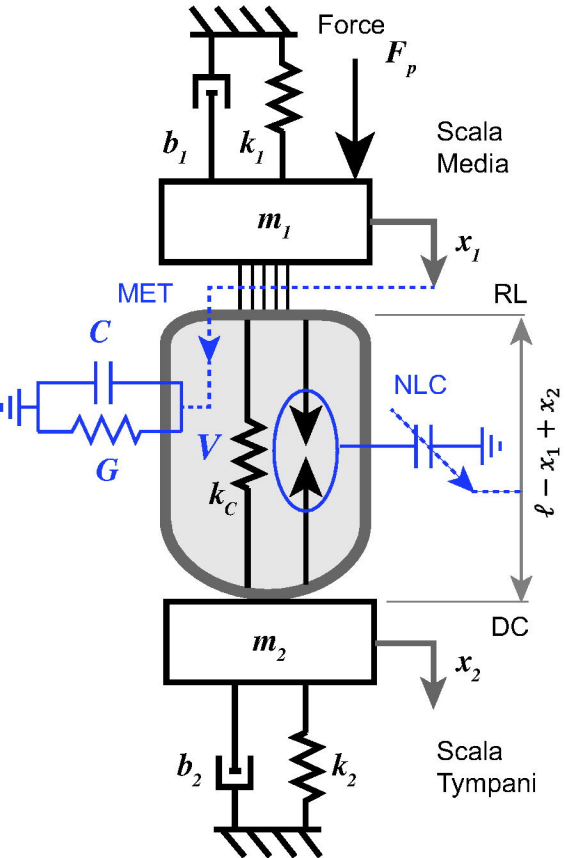
Force
F_p
b_1
k_1
Scala
Media
m_1
x_1
MET
RL
C
NLC
V
G
k_C
$\ell - x_1 + x_2$
DC
m_2
x_2
b_2
k_2
Scala
Tympani

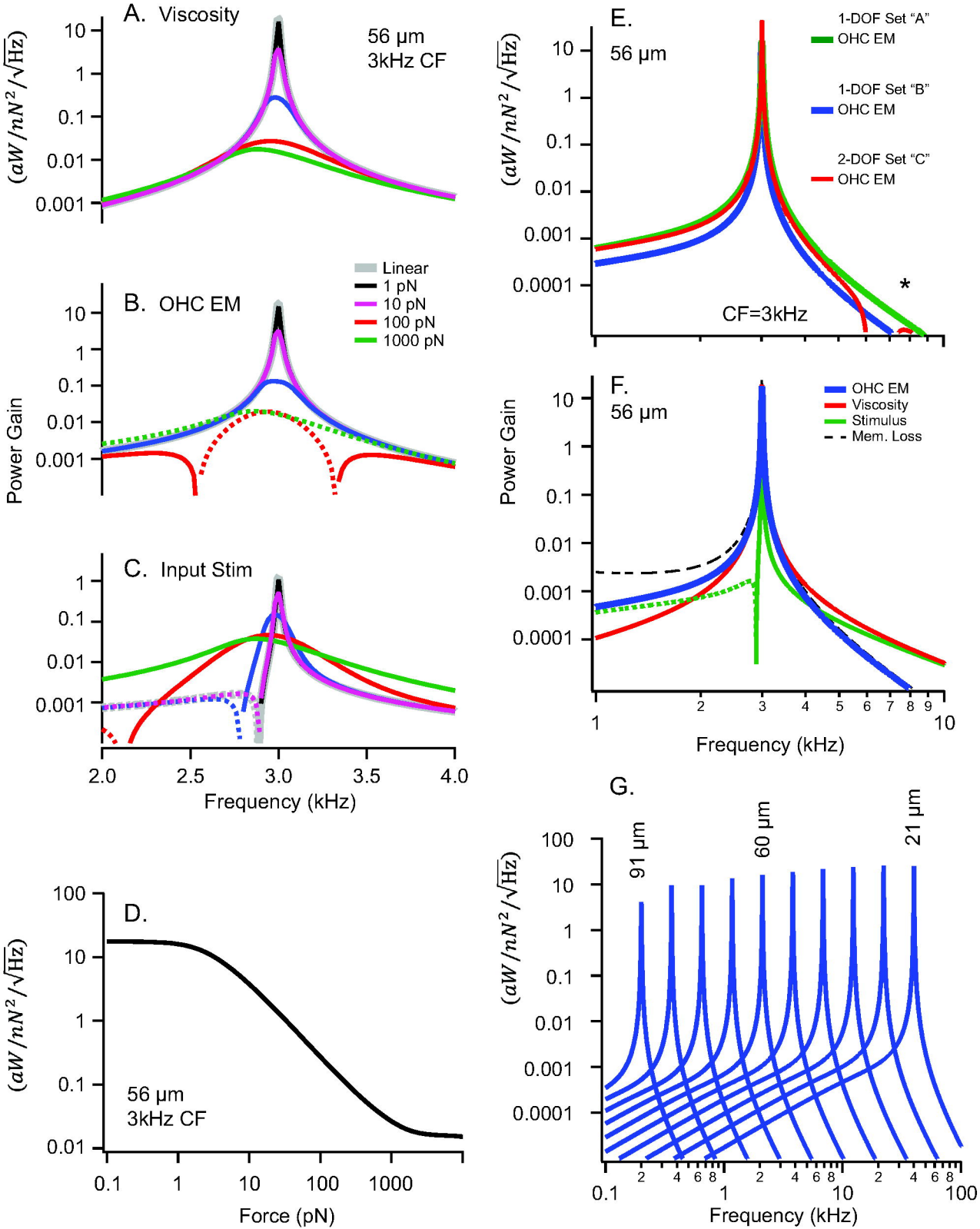
A. Viscosity
56 µm
3kHz CF
B. OHC EM
Linear
1 pN
10 pN
100 pN
1000 pN
C. Input Stim
Power Gain
Frequency (kHz)
D.
56 µm
3kHz CF
Force (pN)
E.
56 µm
1-DOF Set "A"
OHC EM
1-DOF Set "B"
OHC EM
2-DOF Set "C"
OHC EM
CF=3kHz
F.
56 µm
OHC EM
Viscosity
Stimulus
Mem. Loss
Power Gain
Frequency (kHz)
G.
91 µm
60 µm
21 µm
Frequency (kHz)

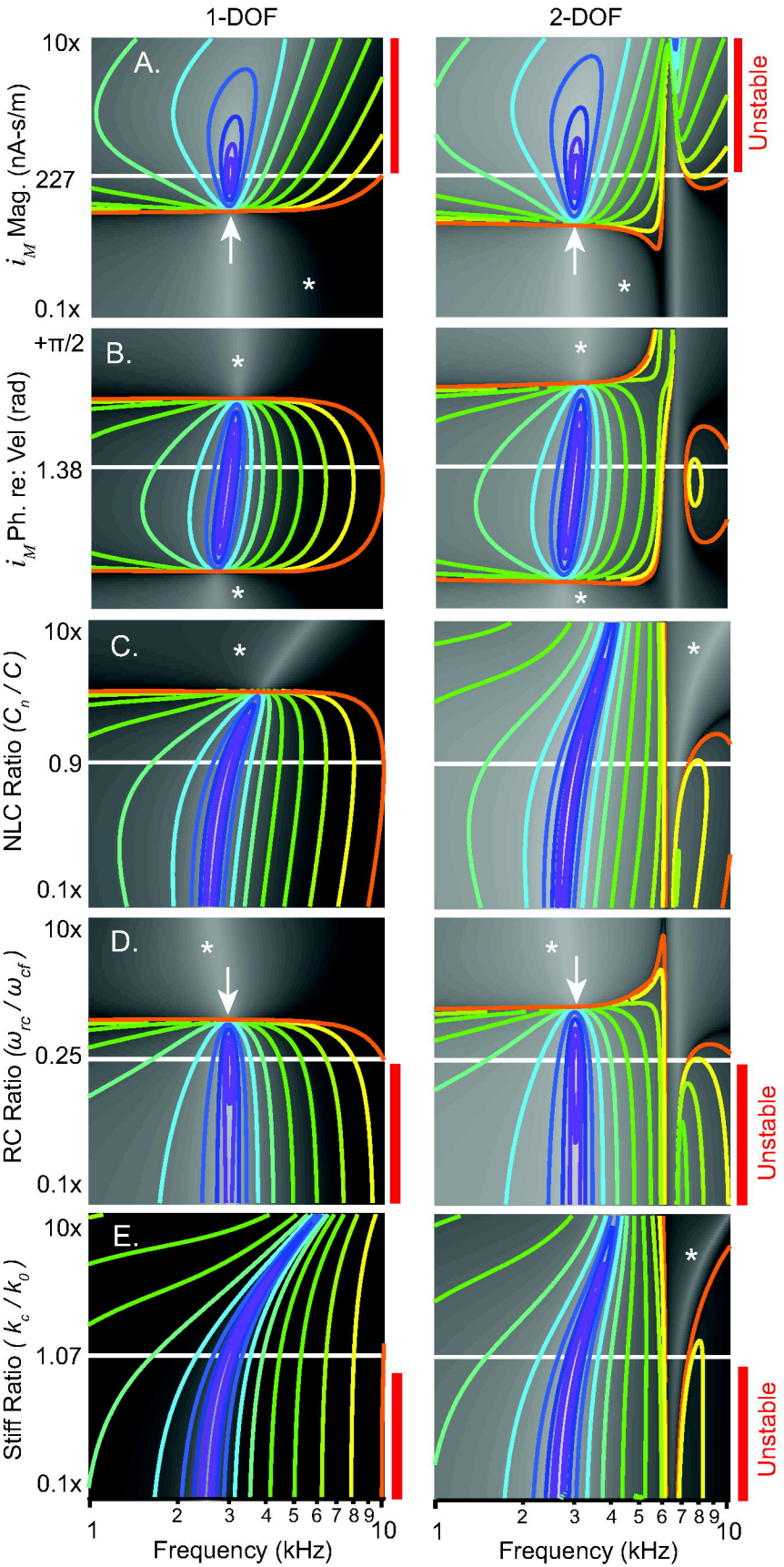
1-DOF
2-DOF
A.
B.
C.
D.
E.
10x
227
0.1x
+π/2
1.38
0.9
0.25
1.07
i_M Mag. (nA-s/m)
i_M Ph. re: Vel (rad)
NLC Ratio (C_n / C)
RC Ratio (ω_{rc} / ω_{cf})
Stiff Ratio (k_c / k_0)
Unstable
1
2
3
4
5
6
7
8
9
10
Frequency (kHz)

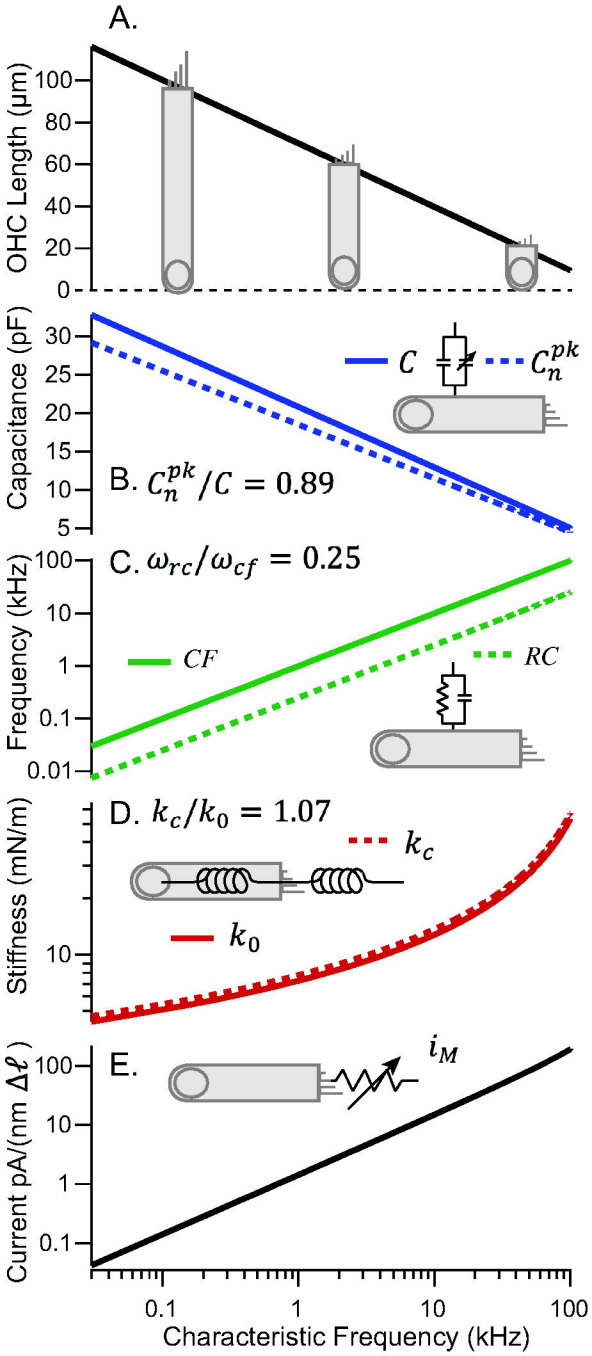
A.
OHC Length (μm)
100
80
60
40
20
0
Capacitance (pF)
30
25
20
15
10
5
C
C_n^{pk}
B. $C_n^{pk}/C = 0.89$
C. $\omega_{rc}/\omega_{cf} = 0.25$
Frequency (kHz)
100
10
1
0.1
0.01
CF
RC
D. $k_c/k_0 = 1.07$
Stiffness (mN/m)
10
k_c
k_0
E.
i_M
Current pA/(nm $\Delta\ell$)
100
10
1
0.1
0.1
1
10
100
Characteristic Frequency (kHz)

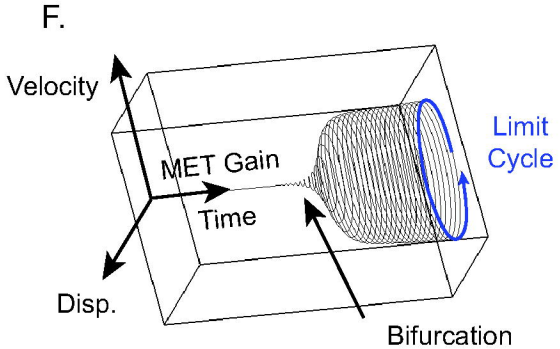
F.
Velocity
MET Gain
Time
Disp.
Limit
Cycle
Bifurcation